DISCOVERY OF X-RAY EMISSION FROM THE GALACTIC SUPERNOVA REMNANT G32.8-0.1 WITH *SUZAKU*

Aya Bamba[1], Yukikatsu Terada[2], John Hewitt[3], Robert Petre[3], Lorella Angelini[3], Samar Safi-Harb[4], Ping Zhou[5], Fabrizio Bocchino[6], and Makoto Sawada[1]

[1] Department of Physics and Mathematics, Aoyama Gakuin University 5-10-1 Fuchinobe Chuo-ku, Sagamihara, Kanagawa 252-5258, Japan
[2] Department of Physics, Science, Saitama University, Sakura, Saitama 338-8570, Japan
[3] NASA Goddard Space Flight Center, Greenbelt, MD 20771, USA
[4] Department of Physics and Astronomy, University of Manitoba, Winnipeg MB R3T 2N2, Canada
[5] Department of Astronomy, Nanjing University, Nanjing 210093, China
[6] INAF—Osservatorio Astronomico di Palermo, Piazza del Parlamento 1, I-90134, Palermo, Italy

ABSTRACT

We present the first dedicated X-ray study of the supernova remnant (SNR) G32.8−0.1 (Kes 78) with *Suzaku*. X-ray emission from the whole SNR shell has been detected for the first time. The X-ray morphology is well correlated with the emission from the radio shell, while anti-correlated with the molecular cloud found in the SNR field. The X-ray spectrum shows not only conventional low-temperature ($kT \sim 0.6$ keV) thermal emission in a non-equilibrium ionization state, but also a very high-temperature ($kT \sim 3.4$ keV) component with a very low ionization timescale ($\sim 2.7 \times 10^{9}$ cm^{-3} s), or a hard nonthermal component with a photon index $\Gamma \sim 2.3$. The average density of the low-temperature plasma is rather low, of the order of 10^{-3}–10^{-2} cm^{-3}, implying that this SNR is expanding into a low-density cavity. We discuss the X-ray emission of the SNR, also detected in TeV with *H.E.S.S.*, together with multi-wavelength studies of the remnant and other gamma-ray emitting SNRs, such as W28 and RCW 86. Analysis of a time-variable source, 2XMM J185114.3−000004, found in the northern part of the SNR, is also reported for the first time. Rapid time variability and a heavily absorbed hard-X-ray spectrum suggest that this source could be a new supergiant fast X-ray transient.

Key words: ISM: individual objects (G32.8-0.1, Kes 78) – ISM: supernova remnants – stars: individual (2XMM J185114.3-000004) – stars: neutron – X-rays: ISM

1. INTRODUCTION

Supernova remnants (SNRs) are believed to be the primary sites for cosmic-ray acceleration up to the "knee" of the cosmic-ray spectrum. X-ray observations revealed that shells of several young SNRs are synchrotron X-ray emitters, implying that they are the acceleration sites of particles (Koyama et al. 1995, 1997). On the other hand, the number of SNRs with a synchrotron X-ray emitting shell is limited (Nakamura et al. 2012). Recent very high-energy (VHE) gamma-ray observations with *H.E.S.S.*, *MAGIC*, and *VERITAS* are continually revealing SNRs[7] as sites for energetic particles accelerated at SNR shocks up to the TeV range (Aharonian et al. 2004, 2007, 2009; Albert et al. 2007; Acciari et al. 2010). Furthermore, recent *Fermi* observations show that, not only young, but also middle-aged SNRs are GeV gamma-ray emitters (Abdo et al. 2009a, 2010a, 2010b; Funk 2011). Some of these gamma-ray emitting SNRs are not covered by deep X-ray observations. We need a larger sample of X-ray studied SNRs with GeV and VHE gamma-ray emission to understand the nature of these cosmic-ray accelerators.

G32.8−0.1 (Kes 78) was discovered by Velusamy & Kundu (1974) in the radio band at an 11 cm wavelength. OH masers were detected from the SNR (Green et al. 1997), suggesting an interaction with an adjacent molecular cloud (Koralesky et al. 1998). Observations of ^{12}CO (Zhou et al. 2007; Zhou & Chen 2011) reveal a dense molecular cloud on the eastern side of the SNR. Zhou & Chen (2011) derived a kinematic

distance to the SNR of 4.8 kpc. Significant GeV emission was also found close to this SNR, with 2FGL J1850.7−0014 in the second Fermi source Catalog (Nolan et al. 2012) suggested to be related to G32.8−0.1. More recently, Auchettl et al. (2014) studied G32.8−0.1 using 52 months of data with *Fermi*; however, given the uncertainties in the γ-ray background model and contamination by other nearby sources, they were unable to confirm the excess of GeV emission from the SNR. The third Fermi source catalog (Acero et al. 2015) confirmed the source again and revised the position and its error. A VHE extended gamma-ray source, HESS J1852−000, was found by the *H.E.S.S.* team outside the eastern edge of the remnant (Kosack et al. 2011).[8] This emission partly overlaps with the radio shell of the SNR and with the molecular cloud seen in CO. While the interaction between the SNR and the molecular cloud had been suggested as a plausible scenario for the TeV emission seen with *H.E.S.S.*, an alternative, but less likely, scenario proposed was its association with a pulsar wind nebula (PWN) associated with a nearby pulsar (PSR J1853–0004). The gamma-ray emission from the SNR implies that there is some high-energy activity from this remnant, despite its nature being still unresolved. This SNR therefore provides another example SNR with potential GeV and with VHE gamma-ray emission. In X-rays, the only information we have published so far on the remnant comes from an *XMM-Newton* study of the northern part of the SNR shell (Zhou & Chen 2011). We still lack an X-ray detection of the whole remnant, which is necessary to understand the properties of this SNR and shed light on its multi-wavelength emission.

---

[7] See http://www.physics.umanitoba.ca/snr/SNRcat for a compilation of X-ray and gamma-ray observations of all Galactic SNRs.

[8] http://www.mpi-hd.mpg.de/hfm/HESS/pages/home/som/2011/02/

Table 1
Observation Log

ObsID	Position (J2000)	XIS Exposure (ks)	HXD Exposure (ks)
507035010	(282.8355, −0.0511)	55.1	53.5
507036010	(282.8355, −0.0511)	52.2	50.2

In this paper, we report on the first detailed X-ray imaging and spectroscopy study of the entire SNR, G32.8−0.1, using *Suzaku* (Mitsuda et al. 2007). We also report on a transient source that went into outburst during our observation. The observation's details are summarized in Section 2. A first analysis of the *Suzaku* X-ray data for these sources is presented in Section 3, the results of which are discussed in Section 4.

2. OBSERVATIONS AND DATA REDUCTION

G32.8−0.1 was observed by *Suzaku* with two pointings, on 2011 April 20–22. The coordinates of two pointings are listed in Table 1. *Suzaku* has two active instruments: four X-ray Imaging Spectrometers (XIS0–XIS3; Koyama et al. 2007a), with each at the focus of an X-Ray Telescope (XRT; Serlemitsos et al. 2007), and a separate Hard X-ray Detector (HXD; Takahashi et al. 2007). Only three XISs could be operated for this study due to a problem with XIS2. XIS1 is a back-illuminated CCD, whereas the others are front-illuminated. The XIS instruments were operated in normal full-frame clocking mode with spaced-row charge injection (Nakajima et al. 2008; Uchiyama et al. 2009), whereas the HXD was operated in normal mode. Data reduction and analysis were made with HEADAS software version 6.13 and XSPEC version 12.8.0. The data were reprocessed with the calibration database version 2013 March 05 for XIS, 2011 September 05 for HXD, and 2011 June 30 for XRT.

In the XIS data screening, we followed the standard screening criteria; filtering out data acquired during passage through the South Atlantic Anomaly (SAA), with an elevation angle to the Earth's dark limb below 5°, or with elevation angle to the bright limb below 25° in order to avoid contamination by emission from the bright limb. Table 1 shows the remaining exposure time.

As for the HXD data set, we also followed the standard screening criteria; filtering out data obtained during passage through the SAA, with an elevation angle to the Earth's limb below 5°, and cutoff rigidity smaller than 8 GV. The resultant exposure time for each observation is shown in Table 1. We adopted the LCFIT model of Fukazawa et al. (2009) for the non-X-ray background (NXB) model. The cosmic X-ray background (CXB) flux is estimated from the *HEAO1* results (Boldt & Leiter 1987), and treated as an additional background component.

3. RESULTS

3.1. Images

The XIS 0.5–2.0 keV and 2.0–8.0 keV mosaic images are shown in Figure 1 The vignetting has been corrected in each image using *xissim* (Ishisaki et al. 2007) after subtracting the NXB (Tawa et al. 2008). One can see clearly a clumpy shell-like structure elongated in the north–south direction in the

0.5–2.0 keV band image. On the other hand, the 2–8 keV band image is dominated by a bright point source detected in our observation in the northern part of the remnant. We find that this point source is positionally coincident with the second *XMM-Newton* serendipitous source catalog source, 2XMM J185114.3−000004 (Watson et al. 2009). This source is now cataloged in the 3XMM Data Release 5 (http://xmm-catalog.irap.omp.eu; I. Zolotukhin et al. 2016, in preparation) as 3XMM J1851−000002, with the best position of (R.A., decl.) = (282.80961, −0.00080) with the position error od 0.63 arcsec. In this paper, we stick to the 2XMM name since the SIMBAD database uses only 2XMM source lists.

Figure 2(a) shows archival VLA Galactic Plane Survey (VGPS) continuum data at 1.4 GHz (Stil et al. 2006) together with the 0.5–2 keV *Suzaku*, 0.5–8 keV *XMM-Newton* (Zhou & Chen 2011), and the *Fermi* source region. We highlight in this image that the diffuse X-ray emission detected by *XMM-Newton* is the northern part of the SNR shell. As seen in Figure 2(a), the X-ray emission traces the radio shell emission; in particular, the *Suzaku* emission follows the morphology of the elongated bright radio emission in the southern part of the remnant.

Figure 2(b) shows the ^{12}CO ($J = 1–0$) image in the velocity range of 80–84 km s^{-1} taken by the Purple Mountain Observatory at Delingha (PMOD) in China (Zhou & Chen 2011), with the 0.5–2 keV *Suzaku* image and the *Fermi* source region overlapped. This image reveals the molecular cloud emission surrounding the X-ray shell. We note that the dent seen in the eastern part of the shell is likely caused by the interaction between the SNR and the molecular cloud. On the other hand, the elongation toward the south may be caused by the expansion of the shell into a relatively lower density medium void of the molecular cloud. The position of the GeV emission is on the western part, and, although the position error is large, there is no overlap between the GeV source and the molecular cloud plus X-ray emission to its east (Acero et al. 2015).

3.2. Spectra of Diffuse Emission

Here, we present our spatially resolved spectroscopic study of the diffuse emission below 10 keV with XIS. We divided the remnant into two parts (north and south) and selected a nearby background region, as shown in Figure 1.

3.2.1. Background Spectrum

The simplest way to determine the background estimation in the source regions is to subtract the spectrum extracted from the background region, but this sometimes introduces an uncertainty due to vignetting. We thus reproduce the background spectrum in the source region as described next.

The background emission contains the NXB, plus the CXB, galactic ridge X-ray emission (GRXE), and emission from the local hot bubble (LHB). The first component is uniform in the field of view, whereas the others are affected by vignetting. The NXB in the background region is generated by xisnxbgen (Tawa et al. 2008), and was subtracted from the spectrum after adjusting the normalization above 10 keV, where we expect no emission except for the NXB.

The NXB-subtracted spectra is shown in Figure 3. We fit it with an absorbed CXB + GRXE + LHB model. To reproduce
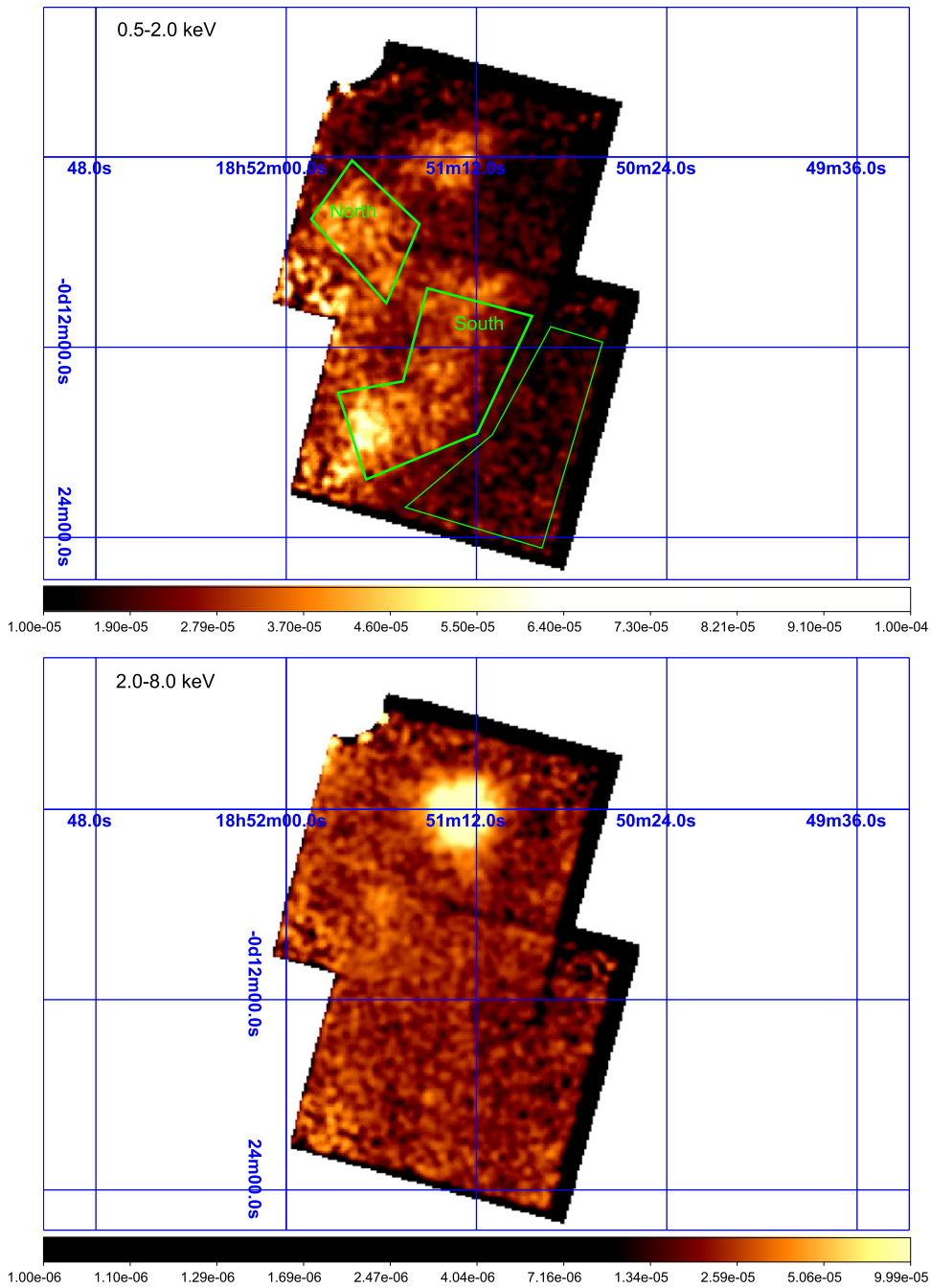
Figure 1. (Top) 0.5–2.0 keV and (bottom) 2.0–8.0 keV band images of the SNR G32.8−0.1. These images were smoothed using a Gaussian filter of Kernel = 0.4 arcmin. Thick and thin green regions represent the source and background regions for the spectral analysis, respectively. The bright point source clearly visible in the hard band on the northwest of the remnant is 2XMM J185114.3−000004.

the CXB emission, we assumed the power-law shape with a photon index of 1.4, and the surface brightness in the 2–10 keV band of 5.4×10^{-15} erg s^{-1} cm^{-2} arcmin^{-2} (Ueda et al. 1999). Note that the background region has an area of 73.7 arcmin^2. The hydrogen column density of the CXB in this direction was fixed to 1.82×10^{22} cm^{-2}, as determined by H I observations (Dickey & Lockman 1990). We also added an absorbed thermal *apec* component for the emission from the LHB (Yoshino et al. 2009), and an absorbed two-temperature *apec* component for the GRXE emission (for example, Koyama et al. 2007b). The best-fit model and parameters are shown in Figure 3 and Table 2, respectively. The best-fit parameters

are roughly consistent with the known components in other regions (Ryu et al. 2009; Yoshino et al. 2009; Sawada et al. 2011).

Assuming that the background spectrum has the same shape and surface brightness in the background and nearby source regions, we simulate the background spectrum in addition to the NXB spectrum in the source region, using the `fakeit` command in XSPEC. We assumed a similar exposure for the simulated background as for the source spectra. This is a similar method to what is described in Fujinaga et al. (2013). We then use this background spectrum in the following analysis.

3
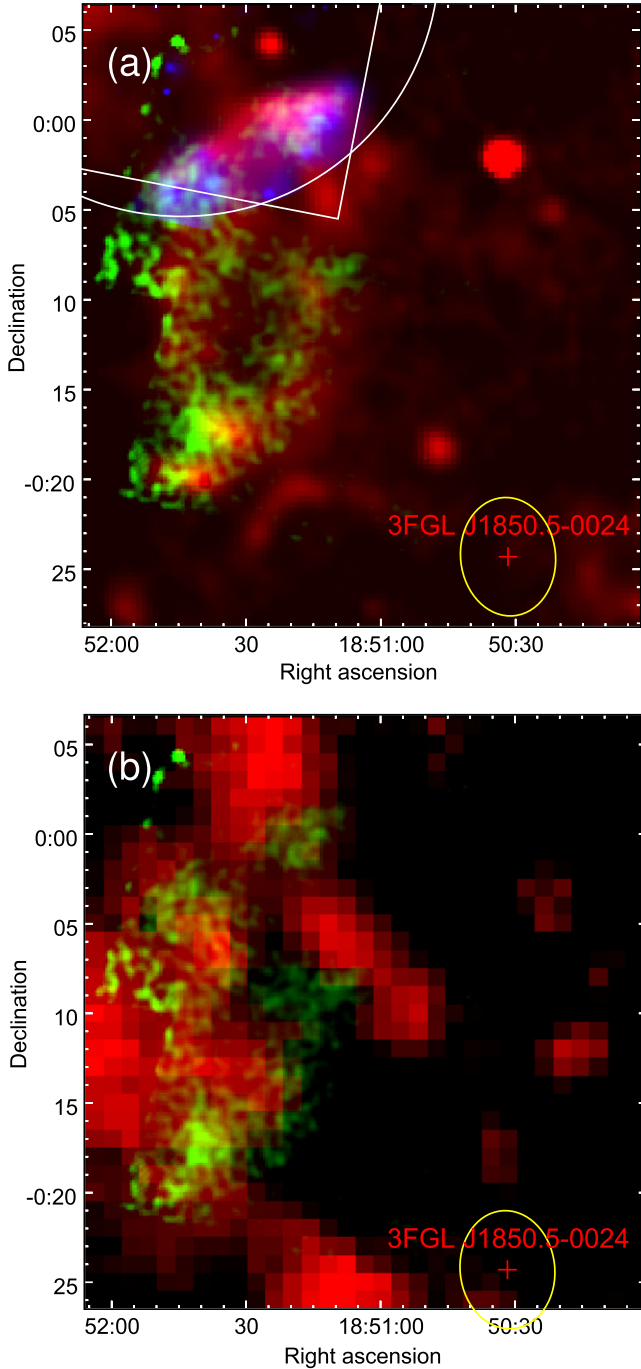
Figure 2. (a) VGPS 1.4 GHz continuum (Stil et al. 2006) (red) together with the 0.5–2 keV *Suzaku* (green), the 0.5–8 keV *XMM* (ObsID = 0017740501; Zhou & Chen 2011) (blue), and the 3FGL source region (Acero et al. 2015) (yellow). The white circle and the box represent the *XMM-Newton* MOS and pn field of views, respectively. (b) PMOD ^{12}CO ($J = 1$–0) image in the velocity range of 80–84 km s^{-1} (Zhou & Chen 2011) (red) with the 0.5–2 keV *Suzaku* (green) and the *Fermi* source region (Acero et al. 2015; yellow).

3.2.2. Source Spectra

We initially perform the spectral analysis of the global SNR using the total emission detected with *Suzaku* from the SNR (i.e., the north+south regions shown in Figure 1).

Figure 4 shows the background-subtracted spectra for the total emission. The spectrum shows emission lines from highly
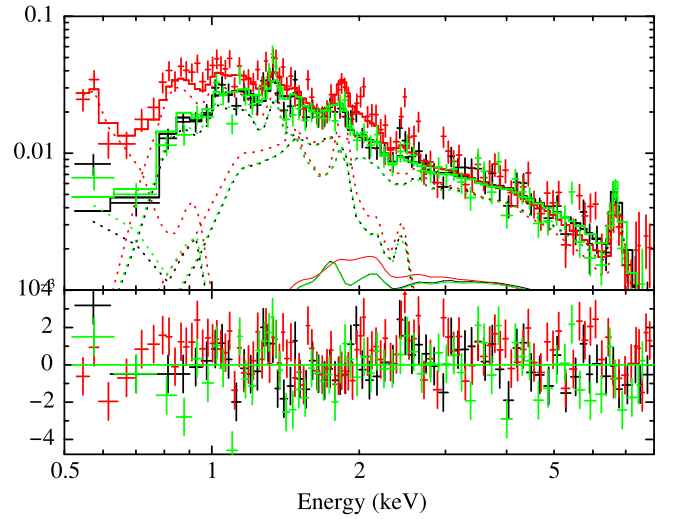
Figure 3. NXB-subtracted spectra of the background region. Black, red, and green crosses represent XIS0, 1, and 3 spectra, respectively. Dotted and thin solid lines represent the thermal and CXB components, respectively.

Table 2
Best-fit Parameters of the Spectral Fitting of the Background Spectra[a]

| Parameters	
CXB Component	
N_H (10^{22} cm^{-2})	1.82 (fixed)
Photon index	1.4 (fixed)
Surface brightness[b]	5.4×10^{15} (fixed)
LHB Component	
N_H (10^{22} cm^{-2})	0.42 (0.14–0.69)
kT (keV)	0.07 (0.04–0.11)
E.M.[c]	0.16 (0.002–6.3)
GRXE Component	
N_H (10^{22} cm^{-2})	0.87 (0.84–0.94)
kT_{low} (keV)	0.59 (0.56–0.62)
E.M.$_{low}$[c]	1.5 (1.2–1.8)
kT_{high} (keV)	6.3 (5.5–7.6)
E.M.$_{high}$[c]	1.1 (1.0–1.2)
χ^2/dof	389.0/236

Notes.
[a] Errors indicate single parameter 90% confidence regions.
[b] In the unit of erg s^{-1} cm^{-2} arcmin^{-2} in 2–10 keV band.
[c] Emission measure in units of $\frac{10^{-17}}{4\pi D^2} \int n_e n_H dV$, where D, n_e, and n_H represent the distance, and electron and hydrogen densities, respectively.

ionized Ne, Mg, and Si, implying that the emission contains a thermal component. We thus fit the spectra initially with an absorbed thermal model from collisionally ionized plasma (`apec` in XSPEC). For the absorption model, we applied the PHABS model, which includes the cross sections of Balucinska-Church & McCammon (1992) with solar abundances Anders & Grevesse (1989). The fit was rejected with a reduced χ^2/ degrees of freedom (dof) of 405.4/122 even when the abundances of metals were treated as free parameters. Introducing a non-equilibrium ionization model (`vnei` and `vvrnei` in XSPEC), we got a better reduced χ^2/dof of 232.0/ 122 and 381.1/123, respectively, but the fit was still rejected. The best fit we found with the `nei` model required a very high temperature, $kT \sim 3.4$ keV, for the SNR as shown in Table 3. This result suggests that the emission contains a hard tail.
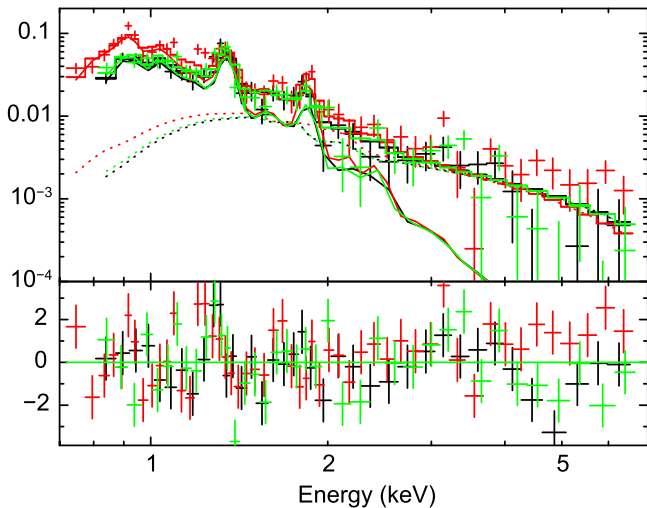
Figure 4. Background-subtracted spectra of the total diffuse emission. Black, red, and green crosses represent XIS0, 1, and 3 spectra, respectively. Solid and dotted lines represent the `vnei` and power-law component, respectively.

We then tried a two-temperature `nei` model and a single temperature `nei` model plus a power-law component. The former model (`nei+nei`) returned a smaller reduced χ^2 of 208.6/122, but required a high temperature (>2 keV) and a small ionization timescale ($n_e t \sim 10^9 \, cm^{-2} \, s$). On the other hand, the (`nei` + power-law) component model, while giving a slightly larger χ^2 of 223.1/121, yielded parameters that are reasonable for X-ray emission from an SNR. With the available data and complications from the background emission, we cannot easily conclude whether the hard tail is thermal or nonthermal, and so we discuss both models in the following section. The best-fit models and parameters are shown in Table 3 and in Figure 4 (for the `vnei`+power-law model).

We have made the same analysis with another plasma model, `vpshock`, and found that the results are basically the same with the same best-fit parameters and reducedχ^2 within errors.

We further verified whether the hard-tail component is real or not. The residuals in the hard-X-ray band remain even when we subtract the background photons accumulated from the background region directly. The background was simulated with the best-fit parameters in the background region fitting (Table 2), which may introduce systematic uncertainty. We tried fitting with another simulated background set with different parameters within the range of Table 2, and found that the results for the source spectra do not change within error. Underestimation of the NXB component can cause such a residual emission, but the NXB count rate in the 3–5 keV (mainly from the power-law component by CXB, Figure 4) is around 10% of that of the total emission, thus it is difficult to consider the hard-tail component as due to the misestimation of the NXB, since the NXB reproduceability is around 10% (Tawa et al. 2008). The possibility of the contamination from the bright and hard northern point source, 2XMM J185114.3 −000004, is unlikely since the best-fit photon index of the diffuse emission is much softer than that of the point source (see Section 3.3). We thus conclude that the hard-tail component most likely originates from the SNR shell.

We also conducted a spatially resolved spectroscopy of the diffuse emission. As shown in Figure 1, we divided the shell into a northern and southern region and extracted spectra for each region. For the background subtraction, we used the simulated background for the total emission (as described above). Due to the limited statistics, we allowed the normalization of `vnei` and power-law components to vary, but the other parameters were fixed to the best-fit value of the total emission. The best-fit models and parameters are shown in Figure 5 and Table 4, respectively. The fitting gave a similar reduced χ^2/dof to the total emission, even with the smaller number of the free parameters.

3.3. 2MM J185114.3−000004

3.3.1. Spectral Analysis

It is difficult to judge whether the emission on the 2XMM J185114.3−000004 region is point-like or not due to the contamination of patchy thermal emission (Zhou & Chen 2011). We assume it is a point source in the following analysis, and this assumption is supported by the time variability as shown in Section 3.3.2. We extracted the source photons from a 3 arcmin radius region. The background region is the source-free region common to the diffuse emission analysis. The background-subtracted spectrum is shown in Figure 6. Below ~3 keV, we see line emission, which we believe is associated with contamination from the thermal emission of the SNR. This emission is very difficult to subtract correctly due to its patchy distribution. We thus used only the 3–10 keV band for the spectral analysis of the point source, since the diffuse emission is significantly fainter than the point source above 3 keV (see Figures 4 and 6). The spectrum extends up to 10 keV, is heavily absorbed, and shows no line-like emission. An absorbed power-law model was thus adopted as the spectral model. The absorption model includes the cross sections of Balucinska-Church & McCammon (1992) with solar abundance Anders & Grevesse (1989). The power-law model yielded an acceptable fit with a hard photon index, $\Gamma \sim 1.6$, and a reduced χ^2 of 191.5/175. The best-fit parameters are listed in the second column of Table 5. We also checked whether there is any significant iron-line emission. For that, we added a narrow Gaussian model with the center energy of 6.4 keV in the fitting, and found a tight upper-limit on the equivalent width of 15 eV.

3.3.2. XIS Timing Analysis

For the timing analysis of this point source, we also used the 3–8 keV band and extracted photons from a 3 arcmin radius region. The left panel of Figure 7 shows the light curve of 2XMM J185114.3−000004, which reveals a highly time-variable source that decays slowly during the observation. One can also see rapid flares with a timescale of a few hundred seconds. The short flares look rather periodic with a timescale of ~7000 s, but this variability is not significant in our data set with the null hypothesis of 20%. We exclude the thermal wobbling of the satellite as a possible source for the flaring (Uchiyama et al. 2008), since this tentative period is not the same as the *Suzaku* satellite's orbital period (~96 minutes). We conclude that this is real time variability of the source.

In order to examine the spectral changes during the flares, we compared the count rates in each bin of the light curve for the 3–5 keV and 5–8 keV bands (i.e., using bands where the source photons are dominant compared with background photons). The right panel shows the 3–8 keV count rate versus the hardness ratio between these bands. One can see that there is no strong trend, implying that there is no significant spectral change during the flares.

Table 3
Best-fit Parameters of Spectral Fitting of the Total Diffuse Emission Spectra[a]

Parameters	vnei	vnei + vnei	vnei + Power-law
N_H (10^{22} cm^{-2})	0.55 (0.48–0.61)	0.74 (0.71–0.82)	0.59 (0.48–0.71)
kT_1 (keV)	3.1 (2.3–5.0)	0.63 (0.37–0.73)	0.65 (0.44–0.97)
Ne	1 (fixed)	1 (fixed)	1.3 (1.1–1.5)
Mg	0.69 (0.55–0.94)	1 (fixed)	1 (fixed)
Si	0.41 (0.30–0.58)	1 (fixed)	1 (fixed)
Fe	0.22 (0.05–0.57)	1 (fixed)	0.28 (0.13–0.49)
nt (10^{10} cm^{-3} s)	1.3 (1.1–1.6)	19 (11–59)	6.0 (3.5–17.1)
E.M.[b]	5.8 (4.2–7.5)	10 (8.9–26)	10 (5–25)
kT_2 (keV)	…	3.4 (2.2–4.7)	…
nt (10^9 cm^{-3} s)	…	2.7 (1.9–3.4)	…
E.M.[b]	…	5.2 (4.0–9.2)	…
Γ	…	…	2.3 (2.0–2.6)
F_{pow} (10^{-13} erg cm^{-2} s^{-1})[c]	…	…	3.5 (2.8–4.2)
χ^2/dof	232.0/122	208.3/122	223.1/121

Notes.
[a] Errors indicate single parameter 90% confidence regions.
[b] Emission measure in units of $\frac{10^{-10}}{4\pi D^2}\int n_e n_H dV$, where D, n_e, and n_H represent the distance, and electron and hydrogen densities.
[c] In 2–10 keV band.

A coherent pulsation search was also performed, though the time resolution of XIS is only 8 s (Koyama et al. 2007a). No significant pulsations were found in the scanned period range of 16–10^4 s with the null hypothesis of 31%.

3.4. HXD Analysis

We also analyzed the HXD P-I-N type diode (PIN) data set to search for a signal from the source in the energy range above 10 keV. After background (NXB+CXB) subtraction, the remaining count rate in the 15–40 keV band in each observation is $2.4 \pm 0.2 \times 10^{-2}$ cnts s^{-1} for OBSID = 507035010 and $1.4 \pm 0.3 \times 10^{-2}$ cnts s^{-1} for OBSID = 507036010. This is 9.0% and 5.4% of the NXB count rate in this band, respectively. The systematic NXB uncertainty is 3%–5% (Fukazawa et al. 2009), thus we conclude that we detect significant emission from the northern part.

The observing region is on the Galactic plane, thus we have to carefully account for the GRXE. Yuasa et al. (2008) reports that the 12–40 keV HXD PIN count rate of the Galactic center is ~0.5 count s^{-1}. Yamauchi & Koyama (1993) shows that the surface brightness of GRXE is a few percent of that in the GC region, thus the expected count rate is ~10^{-2} count s^{-1}, which is significantly lower than our detection. Moreover, the detection level should be the same in the two observations if the emission is from GRXE. We thus conclude that the emission is not from the GRXE.

Figure 8 shows the PIN 15–20 keV light curve after the subtraction of the NXB. We can see the decay of the emission, which is similar to the light curve of 2XMM J185114.3−000004 below 10 keV (Figure 7). This result confirms that the emission is from 2XMM J185114.3−000004.

We have extracted the PIN spectrum above 10 keV as shown in the left panel of Figure 9. We fit it with an absorbed power-law model. The absorption column density was fixed to 11.0×10^{22} cm^{-2}, under the assumption that the emission is from 2XMM J185114.3−000004. The fit was acceptable with a reduced χ^2 of 12.4/10. The best-fit photon index and flux are 4.2 (1.7–6.7) and 3.3 (2.6–4.1) $\times 10^{-12}$ erg cm^{-2} s^{-1} in the 15–20 keV band, respectively. The photon index is relatively soft, but consistent within the error range of the XIS result on 2XMM J185114.3−000004, which also supports our conclusion on the emission origin. We thus carried out the combined spectral fitting of XIS and PIN for 2XMM J185114.3−000004, which is shown in the right panel of Figure 9. We fit the spectra with an absorbed power-law model again, and the fit was acceptable with a reduced χ^2 of 208.6/183. The best-fit models and parameters are shown in the right panel of Figure 9 and the third column in Table 5. We note that we also attempted an absorbed broken-power-low model, but this model did not improve the fit.

HXD has a good timing capability with a 61 μs time resolution and an accuracy of 1.9×10^{-9} ss^{-1} per day (Terada et al. 2008). We thus search for any coherent pulsations of this source using the PIN data set. We used the 15–20 keV range to maximize the signal-to-noise ratio. After barycentric correction, we used the powspec command in the XRONOS package to search the coherent pulsation. However, we could not detect any coherent signal in the period of 61 μs to 512 s. We also tried the timing analysis with the XIS (3–8 keV) and PIN (15–20 keV) combined, and found no significant signal.

4. DISCUSSION

4.1. Diffuse Emission From the SNR

We have detected the X-ray shell structure from G32.8−0.1 for the first time. The best-fit absorption column of 5.9 (4.8–7.1) $\times 10^{21}$ cm^{-2} is marginally smaller than the absorption column in this direction, 1.5–1.9 $\times 10^{22}$ cm^{-2}. Assuming an average density of 0.5–1 cm^{-3}, the expected distance is in the 1.5–4.6 kpc range. This is roughly consistent with the distance estimated from the CO association. We thus use hereafter 4.8 kpc for the distance to the remnant. The size of the X-ray shell is $14' \times 22'$, which coincides with the radio shell. The physical size and total luminosity are 20×31 pc and ~2×10^{34} erg s^{-1} (0.5–10 keV), assuming the kinematic distance of 4.8 kpc.

Next, we discuss the lower-temperature and hard-tail components separately.
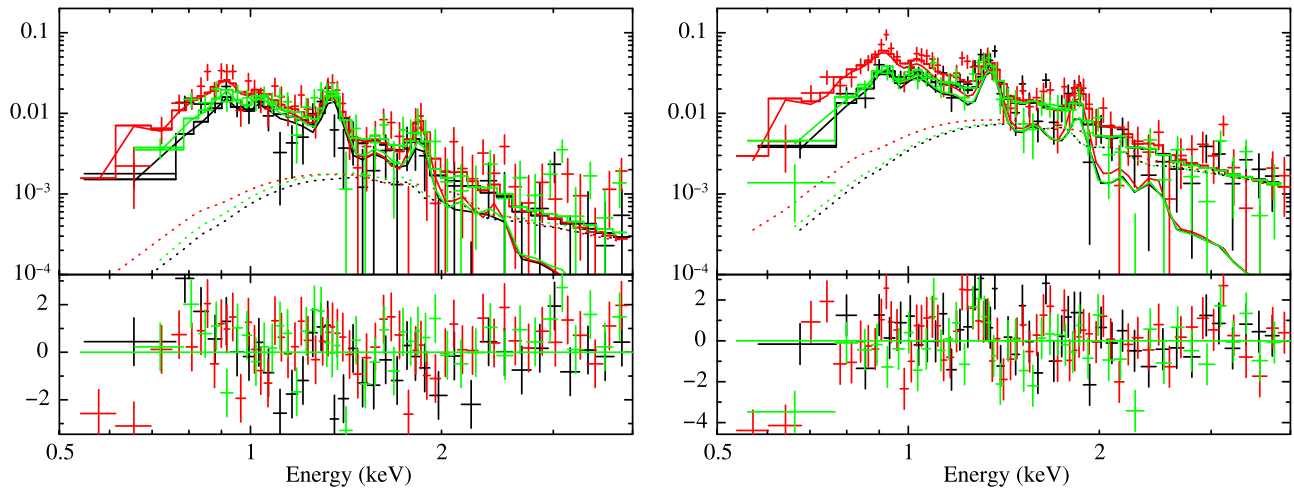
Figure 5. Background-subtracted spectra of the north (left) and south (right) regions. Black, red, and green crosses represent the XIS0, 1, and 3 spectra, respectively. Solid and dotted lines represent `vnei` and power-law component, respectively.

Table 4
Best-fit Parameters of the Spectral Analysis of Northern and Southern Regions of the SNR Shown in Figure 1[a]

Parameters	North	South
`vnei` E.M.[b]	3.8 (3.5–4.1)	6.5 (6.1–6.9)
F_{pow} (10^{-14} erg cm^{-2} s^{-1})[c]	7.4 (4.6–10)	27 (23–30)
χ^2/dof	191.0/134	258.5/154

Notes.
[a] Errors indicate single parameter 90% confidence regions.
[b] Emission measure in units of $\frac{10^{-10}}{4\pi D^2} \int n_e n_H dV$, where D, n_e, and n_H represent the distance, and electron and hydrogen densities, respectively.
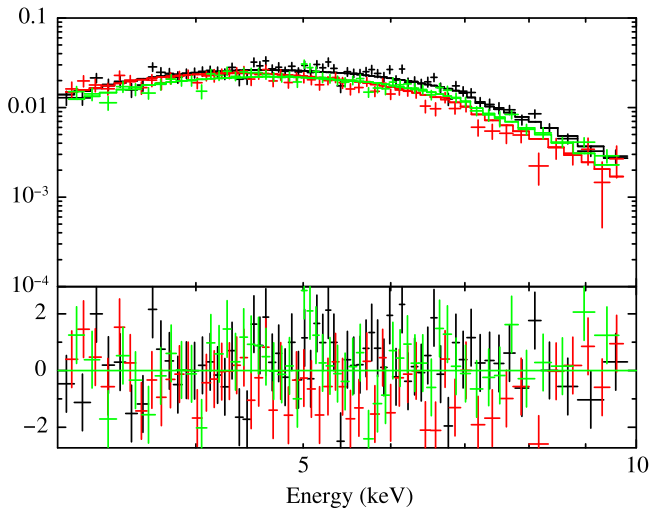[c] In the 2–10 keV band.

Figure 6. Upper panel: background-subtracted XIS spectra of 2XMM J185114.3−000004 in the 3.0–10.0 keV energy band. Lower panel: Residuals from the best-fit models. In both panels, data in black, red, and green represent the XIS0, 1, and 3 spectra, respectively.

4.1.1. Lower-temperature Component

In order to estimate the density and shock age of the low-temperature plasma in this SNR, we assumed that the shape of the emitting plasma is an ellipsoid shell with dimensions of 7, 7, 10 arcmin, with a width of 0.7 arcmin, which correspond to

Table 5
Best-fit Parameters of Spectral Fitting of 2XMM J185114.3−000004[a]

Parameters	XIS Only	XIS + PIN
Γ	1.61 (1.47–1.75)	1.57 (1.44–1.69)
Flux (10^{-12} erg cm^{-2} s^{-1})[b]	9.8 (9.2–10.4)	9.6 (9.0–10.2)
N_H (10^{22} H cm^{-2})	11.0 (9.7–12.2)	10.7 (9.5–11.8)
χ^2/dof	191.5/175	208.6/183

Notes.
[a] Errors indicate single parameter 90% confidence regions.
[b] In the 2–10 keV band.

10, 10, and 15 pc with a width of 1 pc (at the assumed distance of 4.8 kpc). The width of one-twelfth the SNR radius is a rough estimation from the Sedov solution. The total volume is then $4.5 \times 10^{58} D_{4.8\,kpc}^3$ cm^3, where $D_{4.8\,kpc}$ refers to the distance in the unit of 4.8 kpc. Assuming a uniform density over the region, we can derive the average electron density (n_e) from the emission measure as

$$n_e = 8.6 \ (6.1–13.6) \times 10^{-2} f^{-1/2} D_{4.8\,kpc}^{-1/2} \ (cm^{-3}), \quad (1)$$

where f is the volume filling factor and we assumed $n_e = 1.2 \ n_H$. We used the `vnei`+power-law model here (see Table 3; the two-temperature `nei` model will not change our parameter estimate within error). The ambient density n_0 is one-fourth of n_e, thus

$$n_0 = 2.2 \ (1.5–3.4) \times 10^{-2} f^{-1/2} D_{4.8\,kpc}^{-1/2} \ (cm^{-3}). \quad (2)$$

This is a rather low density when compared with interstellar medium and other SNRs even with the smaller distance estimate inferred from the absorption. This is suggestive of expansion of G32.8−0.1 into its progenitor's wind bubble. This is a similar situation to RCW 86, which expands into the wind bubble with the density of $10^{-3}–10^{-2}$ cm^{-3} (Broersen et al. 2014), though RCW 86 is much younger than G32.8−0.1 (Vink et al. 2006). The anti-correlation with the molecular clouds and existence of OH masers further support this scenario. Together with the n_e estimate and the ionization timescale derived from the spectral analysis, we can estimate the shock age of this plasma. Adopting n_e of
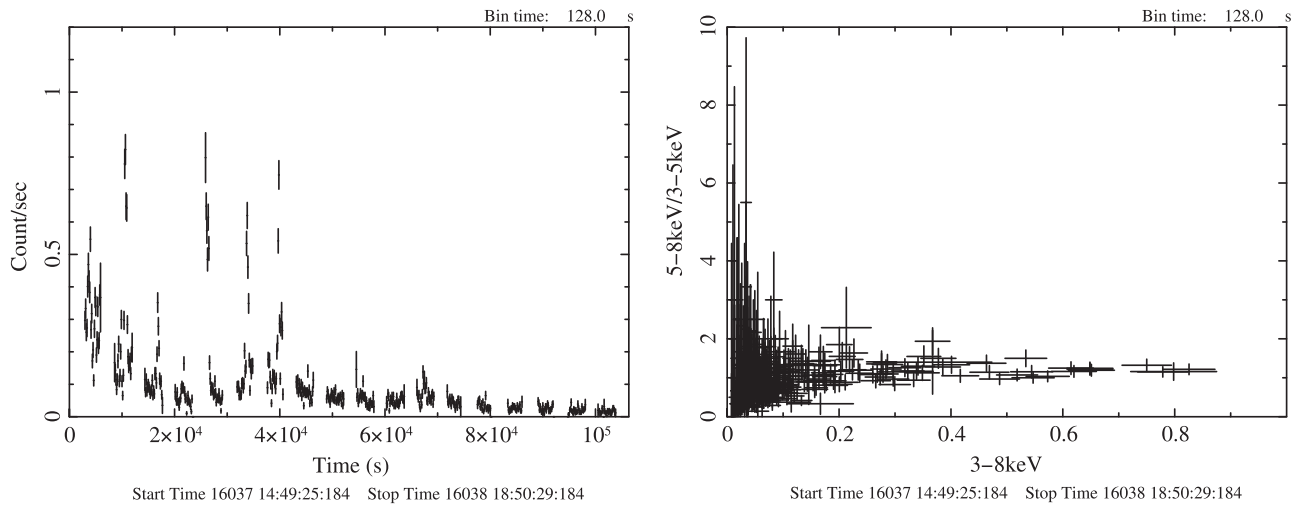
Figure 7. Left: the 3.0–8.0 keV light curve of 2XMM J185114.3−000004. Right: 3–8 keV count rate vs. hardness ratio between 5–8 keV and 3–5 keV. Bin time is 128 s in each panel.
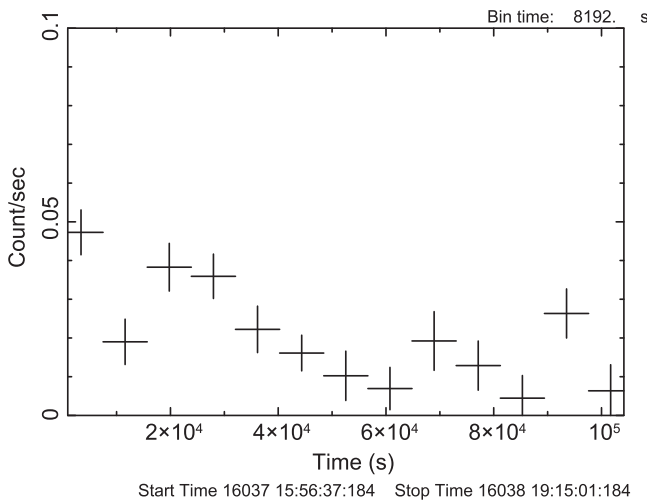
Figure 8. PIN 15–20 keV light curve in the OBSID = 507035010 observation. Bin time is 8192 s.

$8.6 \times 10^{-2} f^{-1/2} D_{4.8\,\mathrm{kpc}}^{-1/2}$, the resultant shock age (t) becomes

$$2.2 \ (1.3\text{–}6.3) \times 10^4 f^{1/2} D_{4.8\,\mathrm{kpc}}^{1/2} \quad \text{(years),} \qquad (3)$$

which suggests that G32.8−0.1 is a middle-aged SNR. Its low luminosity further supports this conclusion (Long 1983).

In the spatially resolved spectroscopy, we derived the emission measure of thermal emission in the northern and southern regions (Table 4). The surface brightness is similar in each region since the area scale of the northern region is around 40% that of the southern region. Together with the same temperature in these regions, we conclude that there is no substantial difference in their density. Note that our observations did not fully cover the eastern part of the remnant, where the molecular cloud dominates. A more complete mapping of the remnant will reveal a clearer correlation between the morphology of the molecular cloud and that of the SNR.

4.1.2. The Hard-tail Component

We have detected a significant hard-tail from the shell region of G32.8−0.1. In the following, we discuss the origin of this emission.

The first possibility we consider is the contamination of hard point sources in this region, since the *Suzaku* angular resolution is not so excellent, around 2 arcmin in half power diameter. We have checked the *ROSAT* PSPC image in this region and did not find any bright point source in the field. Furthermore, the power-law component is significant in both the southern and northern SNR regions, which would be difficult to explain with point source contribution. We thus conclude that this emission is not from a point source, though we cannot rule out the existence of obscured hard sources.

The second possibility is that it is truly diffuse, but caused (at least partly) by the misestimation of the cosmic background level. As shown in Figure 3, the main background emission above 2 keV is the high-temperature component of the GRXE. The fitting with the two-temperature `vnei` model shows that the temperature is consistent with the high-temperature component of the GRXE. We thus checked whether the power-law component can be explained by the GRXE high-temperature component, and found that we need a 27% increase in the flux of the GRXE's high-temperature component to reproduce this power-law component. It is a slightly higher fluctuation than the dispersion of GRXE (H. Uchiyama 2014, private communication, see also Uchiyama et al. 2013), but we cannot dismiss this possibility. We need more statistics in the hard-X-ray band to distinguish this scenario.

An interesting possibility is a PWN origin. The photon index and luminosity are typical for middle-aged PWNe (Kargaltsev & Pavlov 2008; Mattana et al. 2009). A PWN origin for the *H.E.S.S.* emission from the SNR region has also been suggested (Kosack et al. 2011). However, it is hard to explain both the northern and southern regions having a power-law component; on the other hand, it is possible that at least part of the emission has a PWN origin. High-resolution X-ray observations with *Chandra* will be needed to resolve the emission and find any putative PWN or contaminating hard point sources.

The more interesting possibility is that the hard-tail emission is truly diffuse emission originating from the SNR. In the scenario where the hard-tail is of thermal nature, the high kT and very small ionization timescale ($n_{\mathrm{e}}t$, see Table 3) imply that the plasma was recently heated and has a low density. Similar high kT and small $n_{\mathrm{e}}t$ plasma was found in RCW 86
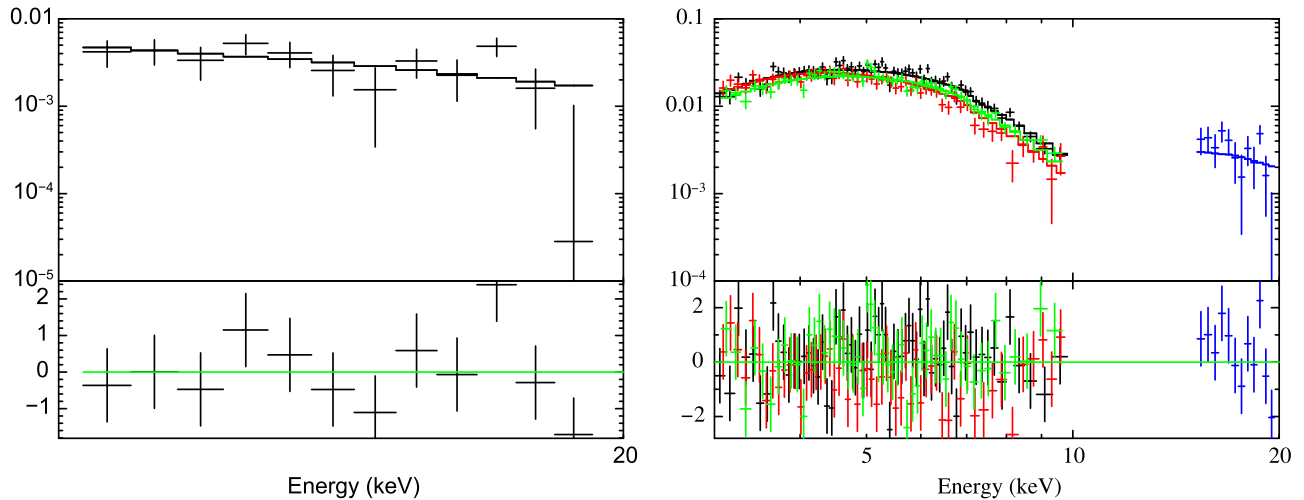
Figure 9. Left panel: the background-subtracted PIN spectrum in the 15–20 keV band. Right panel: the wide-band spectra of 2XMM J185114.3−000004. Data in black, red, green, and blue represent XIS0, 1, 3, and PIN spectrum. In both panels, the lower panels show the residuals from the best-fit model.

(Yamaguchi et al. 2011); it is the ejecta heated by the reverse shock very recently. This may be the case of G32.8−0.1, though it is much older than RCW 86 assuming the latter is associated with SN 185 (Vink et al. 2006). This scenario fits the multi-wavelength observations, and is consistent with the picture that the SNR is expanding into a cavity and has recently hit the molecular cloud.

Next we consider the nonthermal interpretation of the hard tail as originating from the SNR shell. Shocks of SNRs accelerate particles up to 10^{12} eV, and accelerated electrons emit synchrotron X-rays (Koyama et al. 1995). The power-law component in G32.8−0.1 can be the synchrotron emission from accelerated electrons. This scenario is supported by the TeV detection. The luminosity of the hard component, $9.7 \times 10^{32} D_{4.8\ \mathrm{kpc}}^2$ in the 2–10 keV band, however, is rather small for synchrotron X-rays from young SNRs (10^{32}–10^{36} erg s^{-1} in the 2–10 keV band; Nakamura et al. 2012), which further supports the middle-aged scenario. An explosion in a cavity would keep the shock velocity high for longer, which would then lead to a high maximum energy of electrons (Aharonian & Atoyan 1999; Yamazaki et al. 2006; Zirakashvili & Aharonian 2007). The average shock velocity inferred from the shock age and the SNR radius is 5–7 × 10^7 cm s^{-1}, which is also consistent with a middle-aged SNR and a slower than typical value to emit synchrotron X-rays (noting that recent estimates for the shock speeds in RCW 86 give values ranging from 700 to 2200 km s^{-1}, Helder et al. 2013). Since synchrotron X-rays from shocked plasma are expected to have very thin filament-like structures (Bamba et al. 2003, 2005; Vink & Laming 2003), X-ray observations with excellent spatial resolution, such as with *Chandra*, are needed to confirm this scenario and would further allow for an estimate of the magnetic field.

4.1.3. Comparison with Other SNRs with Gamma-Rays

Several SNRs have been detected in the GeV range by *Fermi* (see Funk 2011 for a review). Their soft GeV emission may suggest the escape of high-energy particles (Ellison & Bykov 2011; Ohira et al. 2011; Telezhinsky et al. 2012; Nava & Gabici 2013). Many of these sources are associated with molecular clouds, and particles accelerated at the shock emit

gamma-rays via pion decay with the dense material in the molecular clouds. Our target G32.8−0.1 is interacting with a molecular cloud (Figure 2), which is further supported by the existence of OH masers (Green et al. 1997). However, the association between the molecular cloud and GeV gamma-ray emission is unclear; the peak of the molecular cloud is in the eastern and northern region whereas the gamma-ray peak is on the western side without any overlap with molecular cloud and X-ray emission. (Figure 2). The VHE TeV gamma-ray emission, on the other hand, coincides with the molecular cloud peak in the eastern part of the SNR, and is therefore likely associated with the SNR.

Here, we introduce two SNRs with gamma-rays, W28 and RCW 86 for a comparison to G32.8−0.1. W28 is a middle-aged SNR with GeV and VHE gamma-rays (Aharonian et al. 2008; Abdo et al. 2009b) detected on the northeastern X-ray shell (Nakamura et al. 2014; Zhou et al. 2014). Nakamura et al. (2014) suggest that the GeV/VHE gamma-ray emission is from high-energy particles that recently escaped from the shock and are interacting with a molecular cloud, also giving rise to OH masers (Frail et al. 1994; Claussen et al. 1997; Hoffman et al. 2005). The X-ray emitting plasma in the shell region is in ionization equilibrium (Nakamura et al. 2014), in contrast to the central emission (Sawada & Koyama 2012). The VHE gamma-rays from G32.8−0.1 may have a similar origin to W28. Zhou et al. (2014) suggest the presence of a hard-X-ray tail in the W28 shell, which may be related to the hard tail in G32.8−0.1. Another example, RCW 86, is a bright shell-like SNR in the radio and X-ray bands (Whiteoak & Green 1996; Bamba et al. 2000) expanding in a cavity (Broersen et al. 2014). This SNR has nonthermal emission in X-rays, GeV, and VHE gamma-rays (Bamba et al. 2000; Aharonian et al. 2009; Yuan et al. 2014), which is similar to our case. On the other hand, we have no information on the molecular cloud interaction. More data for such a sample are needed to understand the multi-wavelength and intrinsic properties of these sources.

Young SNRs with VHE gamma-rays often have no significant thermal X-rays (Koyama et al. 1997; Slane et al. 2001; Bamba et al. 2012), suggesting a low-density environment. Such a low density would keep a fast-moving shock speed for a relatively long time and would accelerate

particles more efficiently. We suggest a similarly low density here for G32.8−0.1.

4.2. 2XMM J185114.3−000004

Barthelmy et al. (2012) reported the *Swift* Burst Alert Telescope detection of the outburst of 2XMM J185114.3−000004 on 2012 June 17 15:46:55 UT. The mean count rate in the promptly available XRT data is 0.56 count s^{-1}, whereas the cataloged count rate of this source is equivalent to approximately 0.013 XRT count s^{-1}. No optical counterpart has been found with the UVOT observation on board *Swift*. We also searched for the infrared counterpart in the 2MASS point source catalog (Skrutskie et al. 2006). The nearest 2MASS source is 2MASS 18511447−0000036, but the separation between these sources is 2.6 arcsec, which is larger than the position error of the 3XMM source (0.63 arcsec) and the 2MASS source (0.08 arcsec). We conclude that the source has no infrared counterpart.

With the assumption that the spectral shape is the same in the *Swift* observation and our observation, we derived the 2–10 keV flux in the *Swift* observation to be 7.7×10^{-11} erg cm^{-2} s^{-1} using webpimms. This is 1.5–1.6 count s^{-1} in the *Suzaku* XIS 3–10 keV band. These values are about one order of magnitude larger than the average flux in the *Suzaku* observation (Table 5), and twice the peak flux (Figure 7).

The absorption column of 2XMM J185114.3−000004 is significantly larger than that of the SNR, implying that this point source is unrelated to the SNR. Assuming a distance of 10 kpc, the intrinsic average luminosity is 1.1×10^{35} erg s^{-1} in the 2–10 keV band. The absorption column is much higher than the total Galactic H I column density toward the source (1.5–1.8×10^{22} cm^{-2}; Kalberla et al. 2005), which implies that the source has a local absorption matter.

Recently, a new class of Galactic transients has been emerging with fast and bright flaring X-ray activity, which is referred to as the supergiant fast X-ray transients (SFXT; Sidoli 2011, for a review). These objects are believed to be high-mass X-ray binaries with (a few-hour long) hard-X-ray spectra, and short and bright flares. The fast and large time variability, and the hard spectra of 2XMM J185114.3−000004, suggest that this source is one of the SFXTs. A rather large luminosity and no strong spectral change further support this scenario (Bamba et al. 2001), although Kawabata Nobukawa et al. (2012) reported the change of hardness in the case of AX J1841.0−0536. Some SFXTs show coherent pulsations from 4.7 s (Bamba et al. 2001) to 1276 s (Walter et al. 2006), but our analysis did not show any evidence for pulsations. The short timescale flares within a few hundreds of second is common in other SFXTs (Walter et al. 2006). The origin of the 7000 s intervals of short flares is unknown. This timescale is not the *Suzaku* orbital period (∼96 minutes, Mitsuda et al. 2007), so it is not an artificial feature. It is longer than the coherent pulsations of other SFXTs, and shorter than their orbital periods (3.3–165 days; Walter et al. 2006; Jain et al. 2009).

Another possibility is a flaring low-mass X-ray binaries (LMXB). Some LMXBs show rapid time variability and hard-X-ray spectra (see, XSS J12270−4859; Saitou et al. 2011; de Martino et al. 2013). However, they show spectral hardening during flares, whereas 2XMM J185114.3−000004 did not show any significant spectral change during its flare.

Furthermore, the spectra of flaring LMXBs are not deeply absorbed, which is also different from our source. Recently, Reig et al. (2012) reported that HMXBs with slow pulsations can be accreting magnetars, and our source can be a similar source. However, such sources show only interstellar absorption, which is not the case here. A gamma-ray binary can be a candidate for our source given their high variabilities and hard spectra. However, these objects show spectral hardening when they become brighter (Kishishita et al. 2009, for example), which is again not in the case of 2XMM J185114.3−000004. In summary, follow-up high-resolution and deep observations are needed to improve our understanding of this intriguing source.

REFERENCES

Abdo, A. A., Ackermann, M., Ajello, M., et al. 2009a, ApJL, 706, L1
Abdo, A. A., Ackermann, M., Ajello, M., et al. 2010a, Sci, 327, 1103
Abdo, A. A., Ackermann, M., Ajello, M., et al. 2010b, ApJ, 712, 459
Abdo, A. A., Ackermann, M., Ajello, M., et al. 2009b, ApJS, 183, 46
Acciari, V. A., Aliu, E., Arlen, T., et al. 2010, ApJ, 714, 163
Acero, F., Ackermann, M., Ajello, M., et al. 2015, ApJS, 218, 23
Aharonian, F. A., Akhperjanian, A. G., Aye, K.-M., et al. 2004, Natur, 432, 75
Aharonian, F., Akhperjanian, A. G., Bazer-Bachi, A. R., et al. 2007, ApJ, 661, 236
Aharonian, F., Akhperjanian, A. G., de Almeida, U. B., et al. 2009, ApJ, 692, 1500
Aharonian, F. A., & Atoyan, A. M. 1999, A&A, 351, 330
Aharonian, F., Akhperjanian, A. G., Bazer-Bachi, A. R., et al. 2008, A&A, 481, 401
Albert, J., Aliu, E., Anderhub, H., et al. 2007, A&A, 474, 937
Anders, E., & Grevesse, N. 1989, GeCoA, 53, 197
Auchettl, K., Slane, P., & Castro, D. 2014, ApJ, 783, 32
Balucinska-Church, M., & McCammon, D. 1992, ApJ, 400, 699
Bamba, A., Koyama, K., & Tomida, H. 2000, PASJ, 52, 1157
Bamba, A., Pühlhofer, G., Acero, F., et al. 2012, ApJ, 756, 149
Bamba, A., Yamazaki, R., Ueno, M., & Koyama, K. 2003, ApJ, 589, 827
Bamba, A., Yamazaki, R., Yoshida, T., Terasawa, T., & Koyama, K. 2005, ApJ, 621, 793
Bamba, A., Yokogawa, J., Ueno, M., Koyama, K., & Yamauchi, S. 2001, PASJ, 53, 1179
Barthelmy, S. D., Baumgartner, W. H., Burrows, D. N., et al. 2012, GCN, 13367, 1
Boldt, E., & Leiter, D. 1987, ApJL, 322, L1
Broersen, S., Chiotellis, A., Vink, J., & Bamba, A. 2014, MNRAS, 441, 3040
Claussen, M. J., Frail, D. A., Goss, W. M., & Gaume, R. A. 1997, ApJ, 489, 143
de Martino, D., Belloni, T., Falanga, M., et al. 2013, A&A, 550, A89
Dickey, J. M., & Lockman, F. J. 1990, ARA&A, 28, 215
Ellison, D. C., & Bykov, A. M. 2011, ApJ, 731, 87
Frail, D. A., Goss, W. M., & Slysh, V. I. 1994, ApJL, 424, L111
Fujinaga, T., Mori, K., Bamba, A., et al. 2013, PASJ, 65, 61
Fukazawa, Y., Mizuno, T., Watanabe, S., et al. 2009, PASJ, 61, 17

Funk, S. 2011, in Talk in TeV particle Astrophysics 2011 (Sweden: AlbaNova Univ. center)
Green, A. J., Frail, D. A., Goss, W. M., & Otrupcek, R. 1997, AJ, 114, 2058
Helder, E. A., Vink, J., Bamba, A., et al. 2013, MNRAS, 435, 910
Hoffman, I. M., Goss, W. M., Brogan, C. L., & Claussen, M. J. 2005, ApJ, 620, 257
Ishisaki, Y., Maeda, Y., Fujimoto, R., et al. 2007, PASJ, 59, 113
Jain, C., Paul, B., & Dutta, A. 2009, MNRAS, 397, L11
Kalberla, P. M. W., Burton, W. B., Hartmann, D., et al. 2005, A&A, 440, 775
Kargaltsev, O., & Pavlov, G. G. 2008, in AIP Conf. Series, Vol. 983, 40 Years of Pulsars: Millisecond Pulsars Magnetars and More, ed. C. Bassa et al. (Melville, NY: AIP), 171
Kawabata Nobukawa, K., Nobukawa, M., Tsuru, T. G., & Koyama, K. 2012, PASJ, 64, 99
Kishishita, T., Tanaka, T., Uchiyama, Y., & Takahashi, T. 2009, ApJL, 697, L1
Koralesky, B., Frail, D. A., Goss, W. M., Claussen, M. J., & Green, A. J. 1998, AJ, 116, 1323
Kosack, K., Chaves, R. C., & Acero, F. 2011, Proc. ICRC, 7, 76
Koyama, K., Kinugasa, K., Matsuzaki, K., et al. 1997, PASJ, 49, L7
Koyama, K., Petre, R., Gotthelf, E. V., et al. 1995, Natur, 378, 255
Koyama, K., Tsunemi, H., Dotani, T., et al. 2007a, PASJ, 59, 23
Koyama, K., Uchiyama, H., Hyodo, Y., et al. 2007b, PASJ, 59, 237
Long, K. S. 1983, Supernova Remnants and their X-ray Emission (Dordrecht: Reidel), 525
Mattana, F., Falanga, M., Götz, D., et al. 2009, ApJ, 694, 12
Mitsuda, K., Bautz, M., Inoue, H., et al. 2007, PASJ, 59, 1
Nakajima, H., Yamaguchi, H., Matsumoto, H., et al. 2008, PASJ, 60, 1
Nakamura, R., Bamba, A., Dotani, T., et al. 2012, ApJ, 746, 134
Nakamura, R., Bamba, A., Sawada, M., et al. 2014, PASJ, 66, 6210
Nava, L., & Gabici, S. 2013, MNRAS, 429, 1643
Nolan, P. L., Abdo, A. A., Ackermann, M., et al. 2012, ApJS, 199, 31
Ohira, Y., Murase, K., & Yamazaki, R. 2011, MNRAS, 410, 1577
Reig, P., Torrejón, J. M., & Blay, P. 2012, MNRAS, 425, 595

Ryu, S. G., Koyama, K., Nobukawa, M., Fukuoka, R., & Tsuru, T. G. 2009, PASJ, 61, 751
Saitou, K., Tsujimoto, M., Ebisawa, K., et al. 2011, PASJ, 63, 759
Sawada, M., & Koyama, K. 2012, PASJ, 64, 81
Sawada, M., Tsuru, T. G., Koyama, K., & Oka, T. 2011, PASJ, 63, 849
Serlemitsos, P. J., Soong, Y., Chan, K.-W., et al. 2007, PASJ, 59, 9
Sidoli, L. 2011, AdSpR, 48, 88
Skrutskie, M. F., Cutri, R. M., Stiening, R., et al. 2006, AJ, 131, 1163
Slane, P., Hughes, J. P., Edgar, R. J., et al. 2001, ApJ, 548, 814
Stil, J. M., Taylor, A. R., Dickey, J. M., et al. 2006, AJ, 132, 1158
Takahashi, T., Abe, K., Endo, M., et al. 2007, PASJ, 59, 35
Tawa, N., Hayashida, K., Nagai, M., et al. 2008, PASJ, 60, 11
Telezhinsky, I., Dwarkadas, V. V., & Pohl, M. 2012, A&A, 541, A153
Terada, Y., Enoto, T., Miyawaki, R., et al. 2008, PASJ, 60, 25
Uchiyama, H., Nobukawa, M., Tsuru, T. G., & Koyama, K. 2013, PASJ, 65, 19
Uchiyama, H., Ozawa, M., Matsumoto, H., et al. 2009, PASJ, 61, 9
Uchiyama, Y., Maeda, Y., Ebara, M., et al. 2008, PASJ, 60, 35
Ueda, Y., Takahashi, T., Inoue, H., et al. 1999, ApJ, 518, 656
Velusamy, T., & Kundu, M. R. 1974, A&A, 32, 375
Vink, J., Bleeker, J., van der Heyden, K., et al. 2006, ApJL, 648, L33
Vink, J., & Laming, J. M. 2003, ApJ, 584, 758
Walter, R., Zurita Heras, J., Bassani, L., et al. 2006, A&A, 453, 133
Watson, M. G., Schröder, A. C., Fyfe, D., et al. 2009, A&A, 493, 339
Whiteoak, J. B. Z., & Green, A. J. 1996, A&AS, 118, 329
Yamaguchi, H., Koyama, K., & Uchida, H. 2011, PASJ, 63, 837
Yamauchi, S., & Koyama, K. 1993, ApJ, 404, 620
Yamazaki, R., Kohri, K., Bamba, A., et al. 2006, MNRAS, 371, 1975
Yoshino, T., Mitsuda, K., Yamasaki, N. Y., et al. 2009, PASJ, 61, 805
Yuan, Q., Huang, X., Liu, S., & Zhang, B. 2014, ApJL, 785, L22
Yuasa, T., Tamura, K.-I., Nakazawa, K., et al. 2008, PASJ, 60, 207
Zhou, J.-J., Zhang, X.-Z., Zhang, H.-B., et al. 2007, ChJAA, 7, 705
Zhou, P., & Chen, Y. 2011, ApJ, 743, 4
Zhou, P., Safi-Harb, S., Chen, Y., et al. 2014, ApJ, 791, 87
Zirakashvili, V. N., & Aharonian, F. 2007, A&A, 465, 695